

Article

Enhancing the Thermoelectric Performance of GeSb_4Te_7 Compounds via Alloying Se

Siyu Wang^{1,2}, Tong Xing^{1,*}, Tian-Ran Wei³, Jiawei Zhang¹, Pengfei Qiu¹, Jie Xiao¹, Dudi Ren¹, Xun Shi^{1,3,*} and Lidong Chen^{1,2}

- ¹ State Key Laboratory of High Performance Ceramics and Superfine Microstructure, Shanghai Institute of Ceramics, Chinese Academy of Sciences, Shanghai 200050, China
² School of Physical Science and Technology, ShanghaiTech University, Shanghai 201210, China
³ State Key Laboratory of Metal Matrix Composites, School of Materials Science and Engineering, Shanghai Jiao Tong University, Shanghai 200240, China
* Correspondence: xingtong@mail.sic.ac.cn (T.X.); xshi@mail.sic.ac.cn (X.S.)

Abstract: Ge-Sb-Te compounds (GST), the well-known phase-change materials, are considered to be promising thermoelectric (TE) materials due to their decent thermoelectric performance. While $\text{Ge}_2\text{Sb}_2\text{Te}_5$ and GeSb_2Te_4 have been extensively studied, the TE performance of GeSb_4Te_7 has not been well explored. Reducing the excessive carrier concentration is crucial to improving TE performance for GeSb_4Te_7 . In this work, we synthesize a series of Se-alloyed GeSb_4Te_7 compounds and systematically investigate their structures and transport properties. Raman analysis reveals that Se alloying introduces a new vibrational mode of GeSe_2 , enhancing the interatomic interaction forces within the layers and leading to the reduction of carrier concentration. Additionally, Se alloying also increases the effective mass and thus improves the Seebeck coefficient of GeSb_4Te_7 . The decrease in carrier concentration reduces the carrier thermal conductivity, depressing the total thermal conductivity. Finally, a maximum zT value of 0.77 and an average zT value of 0.48 (300–750 K) have been obtained in $\text{GeSb}_4\text{Te}_{5.5}\text{Se}_{1.5}$. This work investigates the Raman vibration modes and the TE performance in Se-alloyed GeSb_4Te_7 shedding light on the performance optimization of other GST materials.

Keywords: thermoelectric; GeSb_4Te_7 ; carrier concentration; alloying



Citation: Wang, S.; Xing, T.; Wei, T.-R.; Zhang, J.; Qiu, P.; Xiao, J.; Ren, D.; Shi, X.; Chen, L. Enhancing the Thermoelectric Performance of GeSb_4Te_7 Compounds via Alloying Se. *Materials* **2023**, *16*, 3368. <https://doi.org/10.3390/ma16093368>

Academic Editors: Shakeel Ahmad Khandy and Ishtihadah Islam

Received: 19 March 2023

Revised: 9 April 2023

Accepted: 14 April 2023

Published: 25 April 2023



Copyright: © 2023 by the authors. Licensee MDPI, Basel, Switzerland. This article is an open access article distributed under the terms and conditions of the Creative Commons Attribution (CC BY) license (<https://creativecommons.org/licenses/by/4.0/>).

1. Introduction

Thermoelectric (TE) materials enable the direct interconversion of heat and electricity, which is extensively applied in the field of energy harvesting and device cooling [1–4]. The heat–electricity energy conversion efficiency is related to the dimensionless figure of merit zT ($zT = S^2\sigma/\kappa$) of TE material, where T is the absolute temperature, S is the Seebeck coefficient, σ is the electrical conductivity, and κ is the thermal conductivity consisting of the lattice thermal conductivity (κ_L) and carrier thermal conductivity (κ_c) [5–7]. An ideal thermoelectric material should possess high S and large σ , combined with poor κ [8–11]. However, these electrical and thermal transport parameters are coupled with each other, so it is difficult to improve zT for optimizing them simultaneously. Therefore, a lot of research strategies for decoupling these parameters have been proposed to achieve high zT of TE materials [3,9–12].

As the pseudo-binary alloys of IV-VI and V_2 -VI₃ tellurides, Ge-Sb-Te compounds (GSTs) have been widely used in rewritable storage techniques and are receiving more and more attention as TE materials. Metastable cubic and stable hexagonal phases are the two most common crystalline phases of GSTs. Due to their narrow band gap, excellent electrical conductivity, and low lattice thermal conductivity, stable hexagonal phase GSTs are the promising TE candidates, which exhibit anisotropic thermoelectric properties because of their layered structure [13]. In the previous works, $\text{Ge}_2\text{Sb}_2\text{Te}_5$ and GeSb_2Te_4 have been widely studied and optimized to achieve excellent TE performance. By introducing

resonance energy levels through In-doping, Hu et al. increased the effective mass of $\text{Ge}_2\text{Sb}_2\text{Te}_5$ and obtained a maximum zT value of 0.78 at 700 K [14]. Moreover, the electrical properties of $\text{Ge}_2\text{Sb}_2\text{Te}_5$ can also be successfully improved by modulation at the anion site [15,16]. For the GeSb_2Te_4 single crystal, In-doping also introduces an impurity band and results in the locally distorted density of states, which contributes to the enhanced Seebeck coefficient and improved power factor [17,18]. In the GST materials family, GeSb_4Te_7 gains less attention than $\text{Ge}_2\text{Sb}_2\text{Te}_5$ and GeSb_2Te_4 in view of its poor intrinsic TE performance. GeSb_4Te_7 is a strongly degenerate p-type semiconductor and possesses an excessively high hole carrier concentration, limiting the improvement of TE performance. Our previous study focused on GeSb_4Te_7 and successfully decreased the carrier concentration via alloying the n-type homologous counterpart GeBi_4Te_7 [19]. However, the carrier concentration of GeSb_4Te_7 has not been adjusted to the optimal range, and its TE performance can be further improved.

In this study, we synthesized polycrystalline $\text{GeSb}_4\text{Te}_{7-x}\text{Se}_x$ through melting and SPS sintering and investigated the Raman vibration modes using both experimental and calculated Raman data. Our findings provide new insights into the vibrational modes of GeSb_4Te_7 , including the discovery of a new vibrational mode introduced by Se alloying. This leads to the reduced carrier concentration and improved TE performance of GeSb_4Te_7 . A peak zT of 0.77 at 750 K and an average zT of 0.48 between 300 and 750 K have been realized in $\text{GeSb}_4\text{Te}_{5.5}\text{Se}_{1.5}$, which is 54% higher than that of the pristine GeSb_4Te_7 . This study shows that the modified vibrational modes may provide a powerful strategy to optimize TE performance, making GST compounds to be promising TE materials.

2. Experimental Methods

2.1. Material Synthesis

$\text{GeSb}_4\text{Te}_{7-x}\text{Se}_x$ ($x = 0, 0.1, 0.2, 0.3, 0.5, 0.8, 1.5, 2.0,$ and 2.5) samples were synthesized by the melting–annealing method. Raw materials with high purity, including Ge Shots, Sb Shots, Te Shots, and Se Shots (99.999%, Alfa Aesar), were weighed as designed chemical ratios and sealed in the vacuum quartz tubes. The tubes were heated to 1273 K and kept for 12 h. Next, they were quenched in ice water and annealed at 773 K for 3 days. Finally, the obtained ingots were ground into fine powders and consolidated using spark plasma sintering (SPS, Dr Sinter SPS-2040, Fuji Electronic Industrial Co., Ltd, Saitama, Japan) at 673–723 K for 5 min under a uniaxial pressure of 50 MPa. Pellets with a diameter of 10 mm were obtained, and their densities were higher than 98% of the theoretical density.

2.2. Calculation

The calculations were performed employing the projector augmented wave (PAW) method [20] combined with the generalized gradient approximation (GGA) [21] of the modified Perdew–Burke–Ernzerhof form for solids (PBEsol) [22] and the Vienna Ab initio Simulation Package (VASP) [23]. The crystal structure of GeSb_4Te_7 was obtained from the ICSD database (No. 42875). The space group is $P\bar{3}m1$ and the lattice parameters are $a = 4.21000(2)$ (Å) and $c = 23.65000(80)$ (Å). The crystal structure was fully optimized with a $12 \times 12 \times 2$ Monkhorst–Pack k mesh and a force convergence criterion of $1 \text{ meV } \text{Å}^{-1}$. The phonon vibrational frequencies at the Γ point were calculated in supercells with 300 atoms ($5 \times 5 \times 1$ primitive cells) using the finite displacement method [24], which was implemented by combining VASP and Phonopy [25]. The atomic force calculations were conducted with a $2 \times 2 \times 2$ Γ -centered k -mesh. All calculations were achieved with a plane-wave cutoff energy of 500 eV. A convergence criterion of 1×10^{-6} eV was adopted for the electronic loop.

2.3. Material Characterization

X-ray diffraction with Cu $K\alpha$ radiation (XRD, D/max 2550 V, Rigaku, Tokyo, Japan) was performed to determine the crystal structures. Scanning electron microscopy (SEM, ZEISS supra55, Munich, Germany) equipped with EDS was employed to characterize the

chemical components. The Raman spectrum of the $\text{GeSb}_4\text{Te}_{7-x}\text{Se}_x$ powder samples were recorded on an XploRA ONE-532 (Horiba, Kyoto, Japan). ZEM-3 (Ulac-Riko, Yokohama, Japan) was performed to measure the electrical conductivity (σ) and Seebeck coefficient (S) from 300 K to 750 K [12]. The thermal conductivity (κ) was obtained from the relation $\kappa = \lambda\rho C_p$ [9], where the thermal diffusion coefficient (λ) was obtained using the laser pulse analyzer (LFA457, Netzsch, Selb, Germany); the density (ρ) was measured by the Archimedes drainage method; the heat capacity C_p was calculated by the Dulong–Petit law. The Hall coefficient R_H was obtained by the Physical Property Measure System (PPMS, Quantum Design, San Diego, CA, USA), using an AC magnetic field Hall test in the range -5 T–5 T. The carrier concentration was obtained according to $p_H = 1/eR_H$, and the mobility was calculated based on $\mu_H = \sigma R_H$. The absorption spectra were obtained by measuring the powder samples using UV-Vis spectroscopy (Shimadzu Spectroscopy, UV-3101PC, Kyoto, Japan) at room temperature [8]. The optical band gaps of the samples were calculated from the relationship between the optical band gap and the absorption coefficient $(\alpha h\nu)^{\frac{1}{n}} = B(h\nu - E_g)$ [26].

3. Results and Discussion

3.1. Phase and Crystal Structures

The X-ray diffraction (XRD) patterns of $\text{GeSb}_4\text{Te}_{7-x}\text{Se}_x$ ($x = 0, 0.1, 0.2, 0.3, 0.5, 0.8, 1.5, 2.0$, and 2.5) were obtained at room temperature and are presented in Figure 1a. The diffraction peaks are well identified as belonging to the hexagonal structure ($P\bar{3}m1$) of GeSb_4Te_7 . When the Se content is less than 2.0, no obvious secondary phase is observed within the detection limits. However, impurity peaks appear when $x = 2.5$, indexed to GeSb_2Te_4 . With the increase of Se content, the diffraction peaks gradually shift towards the high angle, attributed to the small atomic radius of Se in comparison with Te. The lattice constants of the $\text{GeSb}_4\text{Te}_{7-x}\text{Se}_x$ samples were obtained by refining the XRD data, as shown in Figure 1b. The a - and c -axis lattice constants both show decreasing trends with increasing Se content, which is consistent with the XRD results. Furthermore, SEM and EDS analyses of $\text{GeSb}_4\text{Te}_5\text{Se}_2$ are shown in Figure S1, confirming that all the elements are homogeneously distributed without obvious secondary phases or enriched phases. These results indicate that Se atoms enter the lattice of GeSb_4Te_7 and substitute the Te atoms.

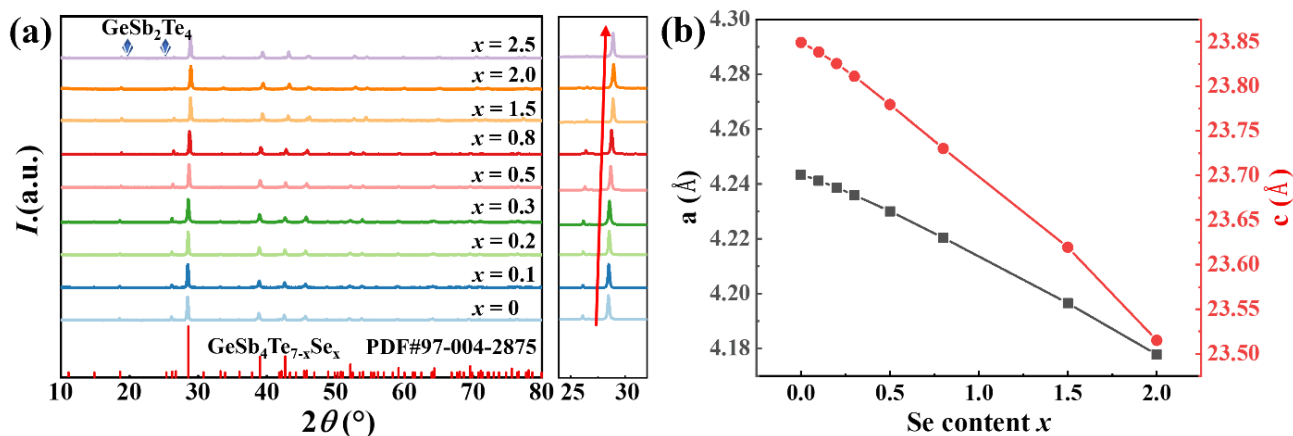


Figure 1. (a) Room temperature X-ray diffraction pattern of powder samples and (b) the lattice constants obtained by refinement as a function of Se content for $\text{GeSb}_4\text{Te}_{7-x}\text{Se}_x$ ($x = 0, 0.1, 0.2, 0.3, 0.5, 0.8, 1.5$, and 2.0).

3.2. Raman Measurement and Analysis

Raman scattering spectroscopy is an effective and highly sensitive tool for characterizing the crystal structure of materials since photons directly couple to the lattice vibrations that reflect the local crystal symmetry. To investigate the effect of Se on the original bonding environment, Raman spectroscopy analysis was conducted to identify the frequency of

bonding vibrational modes among Ge, Sb, Te, and Se atoms. GeSb_4Te_7 possesses a hexagonal phase structure (D_{3d}^3 symmetry) with 10 Raman vibrational modes at the Γ point of the Brillouin zone [27]:

$$\Gamma_{\text{Raman}} = 5A_{1g} + 5E_g, \quad (1)$$

where the A_{1g} and E_g modes correspond to the intralayer and interlayer vibrations along the c -axis and are related to the stretching vibration and the birefringent vibration of atoms in the molecule, respectively (Figures S2 and S3). To study the crystal structure and vibrational modes of GeSb_4Te_7 , we adopted a $5 \times 5 \times 1$ supercell and calculated the theoretical frequencies of Raman vibrational modes employing the density functional theory (DFT), as shown in Table S1. Different from $\text{Ge}_2\text{Sb}_2\text{Te}_5$, GeSb_4Te_7 consists of five-layer Sb_2Te_3 and seven-layer GeSb_2Te_4 along the c -axis (Figure 2a), and thus its Raman vibrational modes can be considered a superposition of several module vibrational modes [28]. The detailed theoretical analysis of Raman vibration modes is described in Supplementary Material.

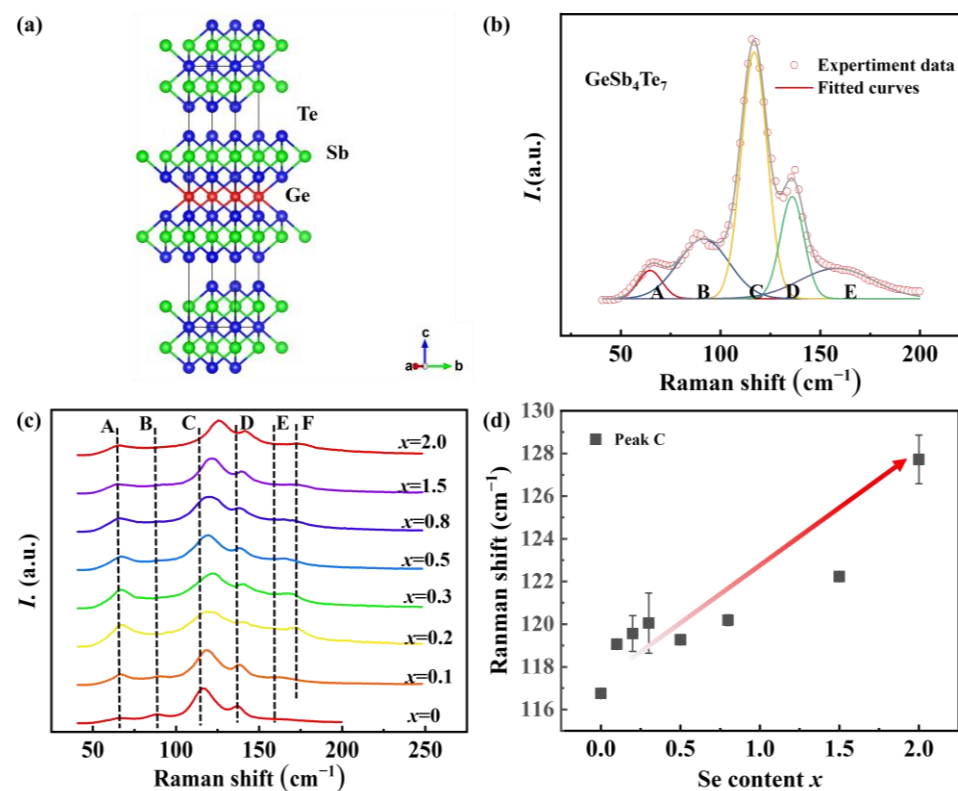


Figure 2. (a) The crystal structure of GeSb_4Te_7 . (b) The experimental Raman spectra of GeSb_4Te_7 and the fitting curve using Gaussian model. (c) The experimental Raman spectra of $\text{GeSb}_4\text{Te}_{7-x}\text{Se}_x$ ($x = 0, 0.1, 0.2, 0.3, 0.5, 0.8, 1.5, \text{ and } 2.0$). (d) The Raman shift of C peak as a function of Se content.

Moreover, we fitted the experimental Raman spectrum of GeSb_4Te_7 using the Gaussian model (Figure 2b), and the detailed values of the fitted parameters are shown in Table S2. The A, B, C, and E peaks of the Raman spectrum for GeSb_4Te_7 correspond to the calculated vibrational modes $A_{1g}(2)$, $E_g(3)$, $A_{1g}(3)$, and $A_{1g}(4)$. The absence of the D peak in the calculated results may be attributed to the anisotropy of GeSb_4Te_7 , which is also observed in the experimental Raman vibrational frequency of MnBi_4Te_7 with a similar structure [28]. The experimental Raman spectra of $\text{GeSb}_4\text{Te}_{7-x}\text{Se}_x$ are presented in Figure 2c. It is indicated that Se-alloying introduces a new Raman vibrational mode with a frequency of approximately $\sim 162 \text{ cm}^{-1}$ (Peak F), which corresponds to the GeSe_2 [29]. With the increase of Se, the C peak generally shifts to the right direction, as plotted in Figure 2d, indicating that Se-alloying enhances the vibrational modes of A_{1g} . This suggests that the substitution of Te by Se enhances the interatomic interactions within the layer and the bond

strength between Ge and Te/Se, which affects the intrinsic Ge vacancy and decreases the hole carrier concentration. A similar phenomenon was observed in S-doped in Cu_2Se [30]. It is noteworthy that the shape of Raman peaks is not changed, implying that the crystal structure and symmetry of GeSb_4Te_7 are scarcely altered via the introduction of Se.

3.3. Thermoelectric Properties

The electrical conductivity (σ), Seebeck coefficient (S), and power factor (PF) of the $\text{GeSb}_4\text{Te}_{7-x}\text{Se}_x$ samples ($x = 0, 0.1, 0.2, 0.3, 0.5, 0.8, 1.5, \text{ and } 2.0$) with the temperature are presented in Figure 3. All samples exhibit positive and metallic conducting behavior. The σ decreases continuously over the entire measured temperature range with the Se content increases. The σ for $\text{GeSb}_4\text{Te}_{5.5}\text{Se}_{1.5}$ is $8.9 \times 10^4 \text{ S m}^{-1}$ at 750 K, which is just about 30% of that for pristine GeSb_4Te_7 . Moreover, Se alloying significantly enhances the Seebeck coefficient of GeSb_4Te_7 . The S for $\text{GeSb}_4\text{Te}_{5.5}\text{Se}_{1.5}$ is around $165 \mu\text{V K}^{-1}$ at 750 K, which is about 140% higher than that of pristine GeSb_4Te_7 . Figure 3d illustrates the S and σ of $\text{GeSb}_4\text{Te}_{7-x}\text{Se}_x$ at 300 K and 700 K as a function of the Se-alloying content. However, the enhancement in S cannot compensate for the reduction in σ , resulting in a continuous decrease of the PF with increasing Se-alloying content at a higher temperature range. As shown in Figure 3c, the maximum PF for $\text{GeSb}_4\text{Te}_5\text{Se}_2$ is $6.8 \mu\text{W cm}^{-1} \text{ K}^{-2}$ at 300 K, about twice that of GeSb_4Te_7 .

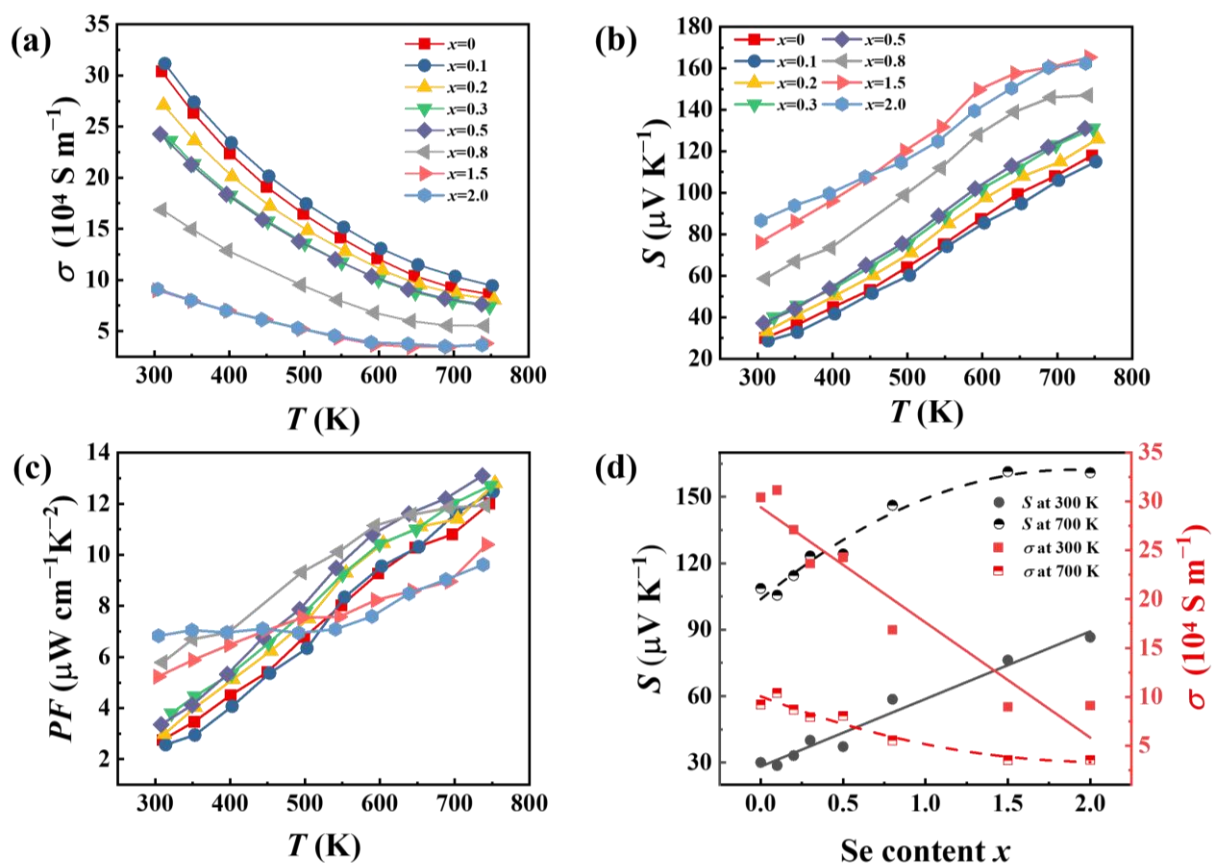


Figure 3. Temperature dependence of (a) electrical conductivity σ , (b) Seebeck coefficient S , and (c) power factor PF for $\text{GeSb}_4\text{Te}_{7-x}\text{Se}_x$ samples ($x = 0, 0.1, 0.2, 0.3, 0.5, 0.8, 1.5, \text{ and } 2.0$). (d) σ and S at 300 K and 700 K as a function of the Se-alloying content.

The carrier concentration (n_{H}) and mobility (μ_{H}) were measured to further understand the electrical transport properties of $\text{GeSb}_4\text{Te}_{7-x}\text{Se}_x$ samples. Upon the introduction of Se into GeSb_4Te_7 , the carrier concentration (n_{H}) at 300 K reduces from $5.8 \times 10^{20} \text{ cm}^{-3}$ to $2.4 \times 10^{20} \text{ cm}^{-3}$, as shown in Figure 4a. This reduction of n_{H} is attributed to the enhanced

interatomic forces within the layer via the introduced vibrational modes of GeSe₂ upon Se alloying. The suppressed n_H is responsible for the decreased electrical conductivity and the enhanced Seebeck coefficient (Figure 3d). However, the carrier mobility (μ_H) hardly changes with increasing Se ($x \leq 0.8$). When the Se content is more than 0.8, the μ_H shows a significant decrease, and it is only $26.0 \text{ cm}^2 \text{ V}^{-1} \text{ s}^{-1}$ for $x = 1.5$, which is approximately 68% of that for the pristine GeSb₄Te₇.

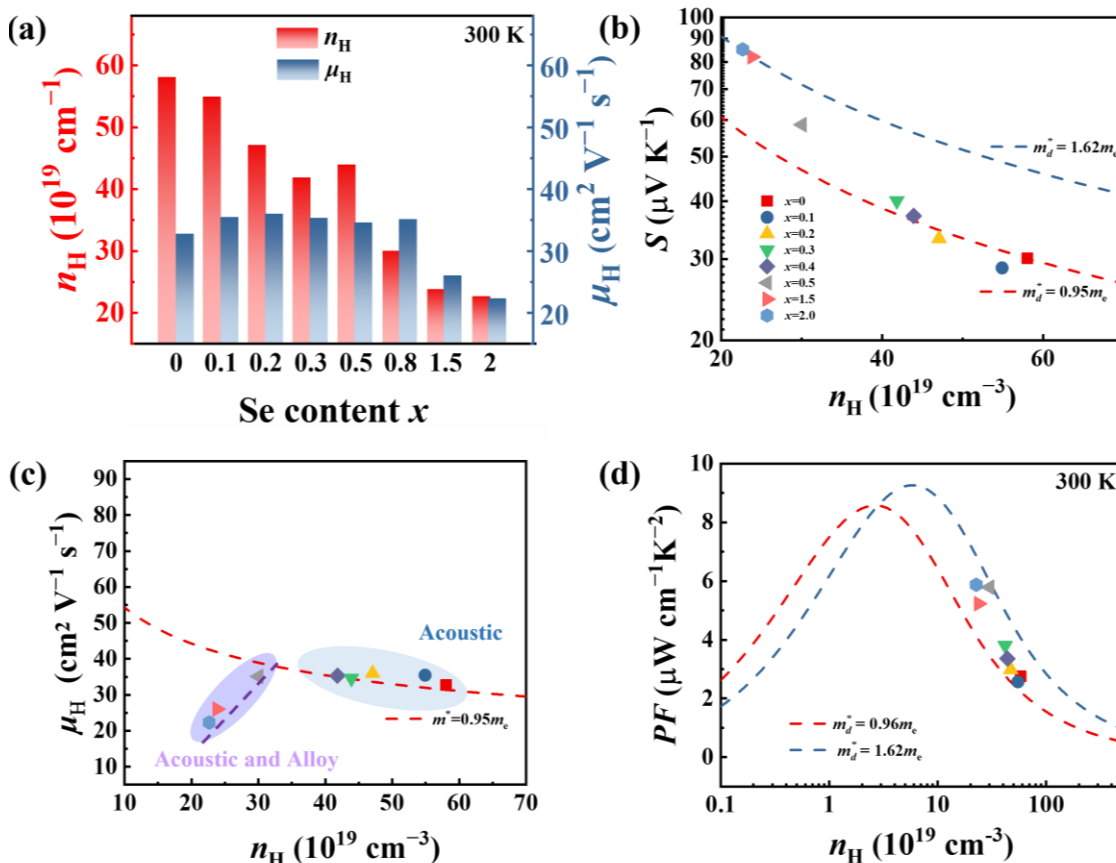


Figure 4. (a) The carrier concentration (n_H) and mobility (μ_H) at room temperature as a function of the Se alloying content. (b) S , (c) μ_H , and (d) PF versus carrier concentration n for GeSb₄Te_{7-x}Se_x at 300 K. The red and blue dashed lines represent the predicted values based on the SPB model with different effective masses.

The single parabolic band (SPB) model was employed to analyze the modification of electrical transport properties for GeSb₄Te_{7-x}Se_x. The transport parameters can be expressed as follows [31–33]:

$$S = \frac{k_B}{e} \left(\frac{2F_1}{F_0} - \eta \right), \tag{2}$$

$$n_H = \frac{8\pi(2m_d^*T)^{\frac{3}{2}}}{3h^3} \frac{2F_0^2}{F_{-1/2}}, \tag{3}$$

$$\mu_H = \mu_0 \frac{F_{-1/2}}{2F_0}, \tag{4}$$

$$PF = S^2 n_H \mu_H e, \tag{5}$$

where η is the reduced Fermi level, $F_i(\eta)$ is the Fermi integral expressed by $F_i(\eta) = \int_0^\infty \frac{x^i dx}{1 + \exp(x - \eta)}$, m^* is the effective mass, e is the elementary charge, k_B is the Boltzmann constant, and h is the Planck constant. Figure 4b plots the Pisarenko relationship (S

vs. n) for $\text{GeSb}_4\text{Te}_{7-x}\text{Se}_x$ ($x = 0, 0.1, 0.2, 0.3, 0.5, 0.8, 1.5, \text{ and } 2.0$). The S decreases with the increasing n_{H} at 300 K. Based on Equations (2) and (3), the Pisarenko curves with different m^* are also plotted in Figure 4b. For the pristine GeSb_4Te_7 , the m^* is $0.95 m_e$ at 300 K (m_e is the free electron mass). The experimental data of all Se-alloyed samples are between two calculated dashed lines with $m^* = 0.92 m_e$ and $1.62 m_e$, which are derived under the single parabolic band (SPB) model [31,32,34]. This indicates that Se-alloying increases the DOS near the Fermi energy level of GeSb_4Te_7 . A similar phenomenon was also observed in Se-alloyed $\text{Ge}_2\text{Sb}_2\text{Te}_5$ [15]. Furthermore, the band gaps of the $\text{GeSb}_4\text{Te}_{7-x}\text{Se}_x$ samples were measured by the optical diffuse reflectance spectrum and listed in Table S4, indicating that Se-alloying affects the band structure and slightly decreases the band gap of GeSb_4Te_7 .

We also investigated the relationship between n and μ_{H} for $\text{GeSb}_4\text{Te}_{7-x}\text{Se}_x$ at 300 K, which is illustrated in Figure 4c. The red dashed line is the theoretical curve considering only acoustic phonon scattering based on the SPB model for $m^* = 0.95 m_e$, and the purple dashed line is the theoretical curve considering acoustic phonon and alloying scattering. For samples with x less than 0.8, acoustic phonon scattering is the dominant scattering mechanism for carriers, and the mobility is calculated based on acoustic phonon scattering following the red dotted line. However, when $x \geq 0.8$, alloying scattering is not negligible anymore, alloying scattering combined with acoustic phonon scattering is considered. When the carriers are dominantly scattered by both acoustic phonons and alloy scattering, μ_0 is provided by [30,35]:

$$\frac{1}{\mu_0} = \frac{1}{\mu_{ac,0}} + \frac{1}{\mu_{al,0}}, \quad (6)$$

$$\mu_{ac,0} = \frac{\pi e \hbar^4 d v_1^2}{\sqrt{2} \Xi^2 m_b^{*5/2} (k_B T)^{3/2}}, \quad (7)$$

$$\mu_{al,0} = \frac{8 e \hbar^4 N_0}{3 \sqrt{2} \pi x (1-x) m_b^{*5/2} (k_B T)^{1/2} U^2}, \quad (8)$$

where $\mu_{ac,0}$ and $\mu_{al,0}$ are the mobilities for acoustic phonon scattering and alloy scattering, respectively. The mobilities of the samples with $x \geq 0.8$ obviously deviate from the red dashed line. The decrease in μ_{H} with increasing Se-alloying content in Figure 4a is attributed to the additional alloy scattering. The PF and n_{H} data for $\text{GeSb}_4\text{Te}_{7-x}\text{Se}_x$ at 300 K are plotted in Figure 4d. The experimental data fall between the theoretical Pisarenko curves with $m^* = 0.95 m_e$ and $m^* = 1.62 m_e$. Se alloying in GeSb_4Te_7 decreases the carrier concentration and achieves higher PF .

In addition to the electrical transport properties, the thermal transport properties of GeSb_4Te_7 are also strongly affected by alloying Se. The thermal conductivities (κ) of all $\text{GeSb}_4\text{Te}_{7-x}\text{Se}_x$ samples are presented in Figure 5a. With the increasing Se alloying content, the κ gradually decreases. The κ of $\text{GeSb}_4\text{Te}_{5.5}\text{Se}_{1.5}$ is approximately $1.2 \text{ W m}^{-1}\text{K}^{-1}$ at 300 K, roughly 43% of GeSb_4Te_7 . Such a reduction is mainly attributed to the suppression of the carrier thermal conductivity (κ_c). The κ_c is calculated based on the Wiedeman–Franz law and presented in Figure 5b ($\kappa_c = L_0 T \sigma$, where L_0 is calculated based on the single parabolic band model) [36–38]. The κ_c decreases with increasing Se alloy content over the temperature range. The lattice thermal conductivities κ_L ($\kappa_L = \kappa - \kappa_c$) of $\text{GeSb}_4\text{Te}_{7-x}\text{Se}_x$ samples are also calculated and presented in Figure S4. The κ_L decreases first and then rises with increasing Se content. A similar phenomenon is observed in the Se-alloyed $\text{Ge}_2\text{Sb}_2\text{Te}_5$ [15]. The minimum κ_L , about $\sim 0.26 \text{ W m}^{-1}\text{K}^{-1}$ at 400 K, is obtained in $\text{GeSb}_4\text{Te}_{6.8}\text{Se}_{0.2}$. The reduction of κ_L is primarily caused by the differences in atomic radii and mass between Te and Se atoms, which introduces a strong strain field and mass fluctuations.

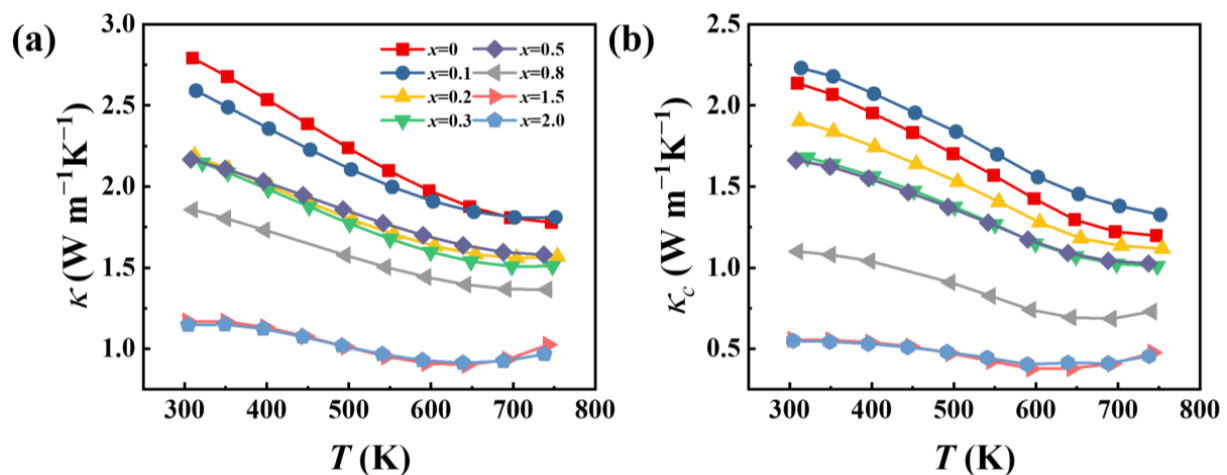


Figure 5. Temperature dependence of (a) thermal conductivity κ and (b) carrier thermal conductivity κ_c for the $\text{GeSb}_4\text{Te}_{7-x}\text{Se}_x$ ($x = 0, 0.1, 0.2, 0.3, 0.5, 0.8, 1.5,$ and 2.0).

The TE figure of merit zT for the $\text{GeSb}_4\text{Te}_{7-x}\text{Se}_x$ samples is presented in Figure 6a. The zT is obviously enhanced upon alloying Se over the entire measured temperature range, attributed to the improved Seebeck coefficient and suppressed thermal conductivity. When $x = 1.5$, a maximum zT value of 0.77 is achieved at 750 K, about 50% higher than that of pristine GeSb_4Te_7 . Moreover, the average zT value within the temperature range 300–750 K for $\text{GeSb}_4\text{Te}_{5.5}\text{Se}_{1.5}$ is 0.48. These values are among the highest values reported in GST compounds, as shown in Figure 6b [13–15,17,19,39].

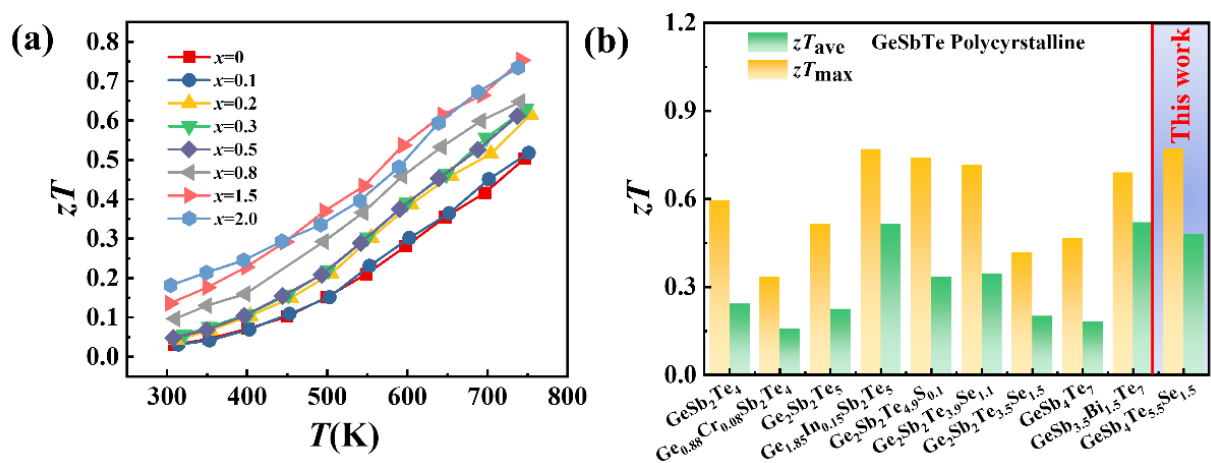


Figure 6. (a) Temperature dependence of TE figure of merit zT for the $\text{GeSb}_4\text{Te}_{7-x}\text{Se}_x$ ($x = 0, 0.1, 0.2, 0.3, 0.5, 0.8, 1.5,$ and 2.0). (b) Comparison of the maximum and average zT values at 300–750 K for several GST compounds and $\text{GeSb}_4\text{Te}_{5.5}\text{Se}_{1.5}$ in this work [13–15,17,19,39].

4. Conclusions

In summary, a series of polycrystalline $\text{GeSb}_4\text{Te}_{7-x}\text{Se}_x$ compounds were synthesized and investigated. Alloying Se suppresses the carrier concentration resulting from the enhancing interatomic interaction forces within the layers via the introduced new Raman vibrational modes. The Seebeck coefficient is improved because of the reduced carrier concentration and enhanced effective mass by Se alloying. In addition, the thermal conductivity is obviously decreased by the simultaneous reduction of κ_L and κ_c . Eventually, $\text{GeSb}_4\text{Te}_{5.5}\text{Se}_{1.5}$ shows a peak zT value of 0.77 at 750 K and an average zT value of 0.48 within the temperature range of 300–750 K. This study deepens the understanding of GeSb_4Te_7 and provides a new approach for optimizing the TE performance of GST compounds via introducing new vibrational modes.

Supplementary Materials: The following supporting information can be downloaded at: <https://www.mdpi.com/article/10.3390/ma16093368/s1>. Figure S1: (a) Backscatter electron (BSE) image, (b) secondary electron (SE2) image of the fractured surface, and energy dispersive spectroscopy (EDS) mappings for (c) Ge, (d) Sb, (e) Te, (f) Se of GeSb₄Te₅Se₂; Figure S2: Sketch of the displacement patterns of Raman-active E_g phonons at the Γ -point for GeSb₄Te₇. Displacements along the c axis are involved; Figure S3: Sketch of the displacement patterns of Raman-active A_{1g} phonons at the Γ -point for GeSb₄Te₇. Displacements along the c axis are involved; Figure S4: Temperature dependence of lattice thermal conductivity κ_L for GeSb₄Te_{7-x}Se_x samples; Figure S5: (a) Mass change and (b) the surface of GeSb₄Te₅Se₂ samples before and after annealing at 750 K; Table S1: Theoretically calculated and measured frequency (cm⁻¹) of g-mode (Raman-active) phonons of the Γ -point phonons for optimized geometry GeSb₄Te₇; Table S2: Peak identity of Raman spectra of GeSb₄Te₇; Table S3: C-peak Raman shifts and linewidths of GeSb₄Te_{7-x}Se_x with different Se contents; Table S4: Direct band gap of hexagonal GeSb₄Te_{7-x}Se_x compounds. References [27,28,40,41] are cited in the supplementary materials.

Author Contributions: In this study, S.W. designed and performed the experiments; J.Z. performed the theoretical calculation; D.R. and J.X. provided guidance for measurements. Data analysis and interpretation were performed by S.W. with the help of T.X., T.-R.W., P.Q. and L.C. The manuscript is revised by T.X., T.-R.W. and X.S. All authors have read and agreed to the published version of the manuscript.

Funding: This work was supported by the National Natural Science Foundation of China (52202330, T2122013), and the Shanghai Pilot Program for Basic Research-Chinese Academy of Science, Shanghai Branch (JCYJ-SHFY-2022-002).

Institutional Review Board Statement: Not applicable.

Informed Consent Statement: Not applicable.

Data Availability Statement: Data is contained within the article or supplementary material.

Conflicts of Interest: The authors declare no conflict of interest.

References

1. Snyder, G.J.; Toberer, E.S. Complex thermoelectric materials. *Nat. Mater.* **2008**, *7*, 105–114. [[CrossRef](#)] [[PubMed](#)]
2. Shi, X.; Chen, L. Thermoelectric materials step up. *Nat. Mater.* **2016**, *15*, 691–692. [[CrossRef](#)] [[PubMed](#)]
3. Wu, Y.; Qiu, P.; Yu, Y.; Xiong, Y.; Deng, T.; Cojocaru-Miréidin, O.; Wuttig, M.; Shi, X.; Chen, L. High-performance and stable AgSbTe₂-based thermoelectric materials for near room temperature applications. *J. Mater.* **2022**, *8*, 1095–1103. [[CrossRef](#)]
4. Qiu, X.; Qiu, P.; Yue, Z.; Chen, H.; Deng, T.; Xiao, J.; Ren, D.; Zhou, Z.; Chen, L.; Shi, X. Phase Transition Behaviors and Thermoelectric Properties of CuAgTe_{1-x}Se_x near 400 K. *ACS Appl. Mater. Interfaces* **2022**, *14*, 1015–1023. [[CrossRef](#)] [[PubMed](#)]
5. He, J.; Tritt, T.M. Advances in thermoelectric materials research: Looking back and moving forward. *Science* **2017**, *357*, eaak9997. [[CrossRef](#)]
6. Shi, X.; Chen, L.; Uher, C. Recent advances in high-performance bulk thermoelectric materials. *Int. Mater. Rev.* **2016**, *61*, 379–415. [[CrossRef](#)]
7. Yang, S.; Gao, Z.; Qiu, P.; Liang, J.; Wei, T.-R.; Deng, T.; Xiao, J.; Shi, X.; Chen, L. Ductile Ag₂₀S₇Te₃ with Excellent Shape-Conformability and High Thermoelectric Performance. *Adv. Mater.* **2021**, *33*, 2007681. [[CrossRef](#)]
8. Shi, X.; He, J. Thermopower and harvesting heat. *Science* **2021**, *371*, 343–344. [[CrossRef](#)]
9. Jiang, B.; Yu, Y.; Cui, J.; Liu, X.; Xie, L.; Liao, J.; Zhang, Q.; Huang, Y.; Ning, S.; Jia, B.; et al. High-entropy-stabilized chalcogenides with high thermoelectric performance. *Science* **2021**, *371*, 830–834. [[CrossRef](#)]
10. Qiu, P.; Cheng, J.; Chai, J.; Du, X.; Xia, X.; Ming, C.; Zhu, C.; Yang, J.; Sun, Y.-Y.; Xu, F.; et al. Exceptionally Heavy Doping Boosts the Performance of Iron Silicide for Refractory Thermoelectrics. *Adv. Energy Mater.* **2022**, *12*, 2200247. [[CrossRef](#)]
11. Zhao, K.; Zhu, C.; Zhu, M.; Chen, H.; Lei, J.; Ren, Q.; Wei, T.-R.; Qiu, P.; Xu, F.; Chen, L.; et al. Structural Modularization of Cu₂Te Leading to High Thermoelectric Performance near the Mott-Ioffe-Regel Limit. *Adv. Mater.* **2022**, *34*, 2108573. [[CrossRef](#)] [[PubMed](#)]
12. Xing, T.; Song, Q.; Qiu, P.; Zhang, Q.; Gu, M.; Xia, X.; Liao, J.; Shi, X.; Chen, L. High efficiency GeTe-based materials and modules for thermoelectric power generation. *Energy Environ. Sci.* **2021**, *14*, 995–1003. [[CrossRef](#)]
13. Wei, T.-R.; Hu, P.; Chen, H.; Zhao, K.; Qiu, P.; Shi, X.; Chen, L. Quasi-two-dimensional GeSbTe compounds as promising thermoelectric materials with anisotropic transport properties. *Appl. Phys. Lett.* **2019**, *114*, 053903. [[CrossRef](#)]
14. Hu, P.; Wei, T.-R.; Qiu, P.; Cao, Y.; Yang, J.; Shi, X.; Chen, L. Largely Enhanced Seebeck Coefficient and Thermoelectric Performance by the Distortion of Electronic Density of States in Ge₂Sb₂Te₅. *ACS Appl. Mater. Interfaces* **2019**, *11*, 34046–34052, Corrected in *ACS Appl. Mater. Interfaces* **2020**, *12*, 7854–7854. [[CrossRef](#)]

15. Hu, P.; Wei, T.-R.; Huang, S.-J.; Xia, X.-G.; Qiu, P.-F.; Yang, J.; Chen, L.-D.; Shi, X. Anion-site-modulated thermoelectric properties in Ge₂Sb₂Te₅-based compounds. *Rare Met.* **2020**, *39*, 1127–1133. [[CrossRef](#)]
16. Du, W.; Gu, Y.; Wang, K.; Yang, X.; Xing, J.; Guo, K.; Luo, J.; Zhao, J.-T. Effective Mass Enhancement and Thermal Conductivity Reduction for Improving the Thermoelectric Properties of Pseudo-Binary Ge₂Sb₂Te₅. *Ann. Phys.* **2020**, *532*, 1900390. [[CrossRef](#)]
17. Chen, P.; Wu, H.; Zhang, B.; Zhou, Z.; Zheng, S.; Dai, L.; Huo, Y.; Zhang, D.; Yan, Y.; Peng, K. Intrinsically Low Lattice Thermal Conductivity and Anisotropic Thermoelectric Performance in In-doped GeSb₂Te₄ Single Crystals. *Adv. Funct. Mater.* **2023**, *33*, 2211281. [[CrossRef](#)]
18. Chen, Y.; Zhang, B.; Zhang, Y.; Wu, H.; Peng, K.; Yang, H.; Zhang, Q.; Liu, X.; Chai, Y.; Lu, X.; et al. Atomic-Scale Visualization and Quantification of Configurational Entropy in Relation to Thermal Conductivity: A Proof-of-Principle Study in t-GeSb₂Te₄. *Adv. Sci.* **2021**, *8*, 2002051. [[CrossRef](#)]
19. Wang, S.; Xing, T.; Hu, P.; Wei, T.-R.; Bai, X.; Qiu, P.; Shi, X.; Chen, L. Optimized carrier concentration and enhanced thermoelectric properties in GeSb_{4-x}Bi_xTe₇ materials. *Appl. Phys. Lett.* **2022**, *121*, 213902. [[CrossRef](#)]
20. Blöchl, P.E. Projector augmented-wave method. *Phys. Rev. B* **1994**, *50*, 17953–17979. [[CrossRef](#)]
21. Perdew, J.P.; Wang, Y. Accurate and simple analytic representation of the electron-gas correlation energy. *Phys. Rev. B* **1992**, *45*, 13244–13249. [[CrossRef](#)] [[PubMed](#)]
22. Perdew, J.P.; Ruzsinszky, A.; Csonka, G.I.; Vydrov, O.A.; Scuseria, G.E.; Constantin, L.A.; Zhou, X.; Burke, K. Restoring the Density-Gradient Expansion for Exchange in Solids and Surfaces. *Phys. Rev. Lett.* **2008**, *100*, 136406. [[CrossRef](#)] [[PubMed](#)]
23. Hafner, J. Ab-initio simulations of materials using VASP: Density-functional theory and beyond. *J. Comput. Chem.* **2008**, *29*, 2044–2078. [[CrossRef](#)] [[PubMed](#)]
24. Parlinski, K.; Li, Z.; Kawazoe, Y. First-principles determination of the soft mode in cubic ZrO₂. *Phys. Rev. Lett.* **1997**, *78*, 4063. [[CrossRef](#)]
25. Togo, A.; Tanaka, I. First principles phonon calculations in materials science. *Scr. Mater.* **2015**, *108*, 1–5. [[CrossRef](#)]
26. López, R.; Gómez, R. Band-gap energy estimation from diffuse reflectance measurements on sol-gel and commercial TiO₂: A comparative study. *J. Sol-Gel Sci. Technol.* **2012**, *61*, 1–7. [[CrossRef](#)]
27. Sosso, G.C.; Caravati, S.; Bernasconi, M. Vibrational properties of crystalline Sb₂Te₃ from first principles. *J. Phys. Condens. Matter* **2009**, *21*, 095410. [[CrossRef](#)]
28. Cho, Y.; Kang, J.H.; Liang, L.; Taylor, M.; Kong, X.; Ghosh, S.; Kargar, F.; Hu, C.; Balandin, A.A.; Puzos, A.A. Phonon modes and Raman signatures of MnBi_{2n}Te_{3n+1} (n = 1, 2, 3, 4) magnetic topological heterostructures. *Phys. Rev. Res.* **2022**, *4*, 013108. [[CrossRef](#)]
29. Zhao, Y.-F.; Guan, Z.; Zhong, N.; Yue, F.-Y.; Xiang, P.-H.; Duan, C.-G. Raman spectra of bulk and few-layer GeSe from first-principles calculations. *Front. Mater.* **2021**, *8*, 736057. [[CrossRef](#)]
30. Zhao, K.; Blichfeld, A.B.; Chen, H.; Song, Q.; Zhang, T.; Zhu, C.; Ren, D.; Hanus, R.; Qiu, P.; Iversen, B.B. Enhanced thermoelectric performance through tuning bonding energy in Cu₂Se_{1-x}S_x liquid-like materials. *Chem. Mater.* **2017**, *29*, 6367–6377. [[CrossRef](#)]
31. Deng, T.; Qiu, P.; Xing, T.; Zhou, Z.; Wei, T.-R.; Ren, D.; Xiao, J.; Shi, X.; Chen, L. A low-cost and eco-friendly Br-doped Cu₇Sn₃S₁₀ thermoelectric compound with zT around unity. *J. Mater. Chem. A* **2021**, *9*, 7946–7954. [[CrossRef](#)]
32. May, A.F.; Snyder, G.J. *Thermoelectrics and its Energy Harvesting*; Rowe, D.M., Ed.; CRC Press: Boca Raton, FL, USA, 2012; pp. 1–18. [[CrossRef](#)]
33. Liu, J.; Xing, T.; Gao, Z.Q.; Liang, J.S.; Peng, L.M.; Xiao, J.; Qiu, P.F.; Shi, X.; Chen, L.D. Enhanced thermoelectric performance in ductile Ag₂S-based materials via doping iodine. *Appl. Phys. Lett.* **2021**, *119*, 121905. [[CrossRef](#)]
34. Deng, T.; Wei, T.-R.; Song, Q.; Xu, Q.; Ren, D.; Qiu, P.; Shi, X.; Chen, L. Thermoelectric properties of n-type Cu₄Sn₇S₁₆-based compounds. *RSC Adv.* **2019**, *9*, 7826–7832. [[CrossRef](#)]
35. Chen, R.; Qiu, P.F.; Jiang, B.B.; Hu, P.; Zhang, Y.M.; Yang, J.; Ren, D.D.; Shi, X.; Chen, L.D. Significantly optimized thermoelectric properties in high-symmetry cubic Cu₇PSe₆ compounds via entropy engineering. *J. Mater. Chem. A* **2018**, *6*, 6493–6502. [[CrossRef](#)]
36. Kim, H.-S.; Gibbs, Z.M.; Tang, Y.; Wang, H.; Snyder, G.J. Characterization of Lorenz number with Seebeck coefficient measurement. *APL Mater.* **2015**, *3*, 041506. [[CrossRef](#)]
37. Xing, T.; Zhu, C.; Song, Q.; Huang, H.; Xiao, J.; Ren, D.; Shi, M.; Qiu, P.; Shi, X.; Xu, F.; et al. Ultralow Lattice Thermal Conductivity and Superhigh Thermoelectric Figure-of-Merit in (Mg, Bi) Co-Doped GeTe. *Adv. Mater.* **2021**, *33*, 2008773. [[CrossRef](#)] [[PubMed](#)]
38. Hao, F.; Qiu, P.; Song, Q.; Chen, H.; Lu, P.; Ren, D.; Shi, X.; Chen, L. Roles of Cu in the Enhanced Thermoelectric Properties in Bi_{0.5}Sb_{1.5}Te₃. *Materials* **2017**, *10*, 251. [[CrossRef](#)]
39. Welzmler, S.; Schlegel, R.; Pöppel, A.; Bothmann, G.; Scheidt, E.-W.; Scherer, W.; Oeckler, O. Doping GeSb₂Te₄ with Cr³⁺: Structure and Temperature-Dependent Physical Properties. *Z. Für Anorg. Und Allg. Chem.* **2015**, *641*, 2350–2356. [[CrossRef](#)]
40. Sosso, G.; Caravati, S.; Gatti, C.; Assoni, S.; Bernasconi, M. Vibrational properties of hexagonal Ge₂Sb₂Te₅ from first principles. *J. Phys. Condens. Matter* **2009**, *21*, 245401. [[CrossRef](#)]
41. Fang, J.; Wang, J.; Cao, X.; Man, Y.; Liu, C.; Cheng, L.; Zhang, X.; Zhao, H.; Zhang, H.; Li, J. Thickness dependence of a giant nonlinear saturable absorption response in GeSb₄Te₇ thin films. *J. Phys. Commun.* **2018**, *2*, 015009. [[CrossRef](#)]

Disclaimer/Publisher’s Note: The statements, opinions and data contained in all publications are solely those of the individual author(s) and contributor(s) and not of MDPI and/or the editor(s). MDPI and/or the editor(s) disclaim responsibility for any injury to people or property resulting from any ideas, methods, instructions or products referred to in the content.